Molecular basis underlying the ciliary defects caused by *IFT52* variations found in skeletal ciliopathies

Yamato Ishida, Koshi Tasaki, Yohei Katoh, and Kazuhisa Nakayama*
Department of Physiological Chemistry, Graduate School of Pharmaceutical Sciences, Kyoto University, Sakyo-ku, Kyoto 606-8501, Japan

ABSTRACT **Bidirectional protein trafficking within cilia is mediated by the intraflagellar transport (IFT) machinery, which contains the IFT-A and IFT-B complexes powered by the kinesin-2 and dynein-2 motors. Mutations in genes encoding subunits of the IFT-A and dynein-2 complexes cause skeletal ciliopathies. Some subunits of the IFT-B complex, including IFT52, IFT80, and IFT172, are also mutated in skeletal ciliopathies. We here show that IFT52 variants found in individuals with short-rib polydactyly syndrome (SRPS) are compromised in terms of formation of the IFT-B holocomplex from two subcomplexes and its interaction with heterotrimeric kinesin-II. *IFT52*-knockout (KO) cells expressing IFT52 variants that mimic the cellular conditions of individuals with SRPS demonstrated mild ciliogenesis defects and a decrease in ciliary IFT-B level. Furthermore, in *IFT52*-KO cells expressing an SRPS variant of IFT52, ciliary tip localization of ICK/CILK1 and KIF17, both of which are likely to be transported to the tip via binding to the IFT-B complex, was significantly impaired. Altogether these results indicate that impaired anterograde trafficking caused by a decrease in the ciliary level of IFT-B or in its binding to kinesin-II underlies the ciliary defects found in skeletal ciliopathies caused by IFT52 variations.**

Monitoring Editor
Gregory Pazour
University of Massachusetts

Received: Jun 2, 2022
Revised: Jun 6, 2022
Accepted: Jun 9, 2022

INTRODUCTION

Primary cilia are microtubule-based, antenna-like structures that sense, transmit, and integrate various mechanical and chemical signals (e.g., fluid flow and Hedgehog [Hh] signaling) that are necessary for embryonic development and tissue homeostasis (Anvarian *et al.*, 2019; Kopinke *et al.*, 2021). To achieve these functions, the composition of proteins on the ciliary membrane and in the ciliary interior are kept distinct from those on the plasma membrane and in the cytoplasm by the barrier function of the ciliary gate, composed of transition fibers and the transition zone (Garcia-Gonzalo and Reiter, 2017; Gonçalves and Pelletier, 2017). The intraflagellar transport (IFT) machinery, containing the IFT-A and IFT-B complexes, mediates bidirectional protein trafficking within cilia and the import and export of proteins across the ciliary gate. Our recent study suggested that heterotrimeric kinesin-II binds to the IFT-B complex, which is composed of 16 subunits, and drives anterograde trafficking along the axonemal microtubules (Funabashi *et al.*, 2018), although heterotrimeric kinesin-II was proposed to carry the IFT-A complex in *Caenorhabditis elegans* sensory cilia (Prevo *et al.*, 2017). IFT-B also participates in the export of ciliary membrane proteins across the ciliary gate together with the BBSome complex (Nachury and Mick, 2019; Nakayama and Katoh, 2020). The IFT-B complex can be divided into the core (IFT-B1) and peripheral (IFT-B2) subcomplexes, which are connected to each other by composite interactions involving two core subunits, IFT52 and IFT88, and two peripheral subunits, IFT38 and IFT57 (see Figure 1A) (Boldt *et al.*, 2016;

This article was published online ahead of print in MBoC in Press (http://www.molbiolcell.org/cgi/doi/10.1091/mbc.E22-05-0188) on June 15, 2022.

Conflict of interest: The authors declare no conflicts of interest associated with this study.

Author contributions: Y.I. designed and performed the experiments; K.T. performed the experiments; and Y.K. and K.N. designed the experiments and prepared the manuscript.

*Address correspondence to: Kazuhisa Nakayama (kazunaka@pharm.kyoto-u.ac.jp).

Abbreviations used: BBS, Bardet–Biedl syndrome; CED, cranioectodermal dysplasia; EGFP, enhanced green fluorescent protein; FBS, fetal bovine serum; GIFT, GldG intraflagellar transport; GPCR, G protein–coupled receptor; GST, glutathione *S*-transferase; Hh, Hedgehog; IFT, intraflagellar transport; hTERT-RPE1, human telomerase reverse transcriptase–immortalized retinal pigment epithelial 1; KO, knockout; Nb, nanobody; SAG, Smoothened Agonist; sgRNA, single-guide RNA; SMO, Smoothened; SRPS, short-rib polydactyly syndrome; WT, wild type.

© 2022 Ishida *et al*. This article is distributed by The American Society for Cell Biology under license from the author(s). Two months after publication it is available to the public under an Attribution–Noncommercial-Share Alike 4.0 International Creative Commons License (http://creativecommons.org/licenses/by-nc-sa/4.0).
"ASCB®," "The American Society for Cell Biology®," and "Molecular Biology of the Cell®" are registered trademarks of The American Society for Cell Biology.

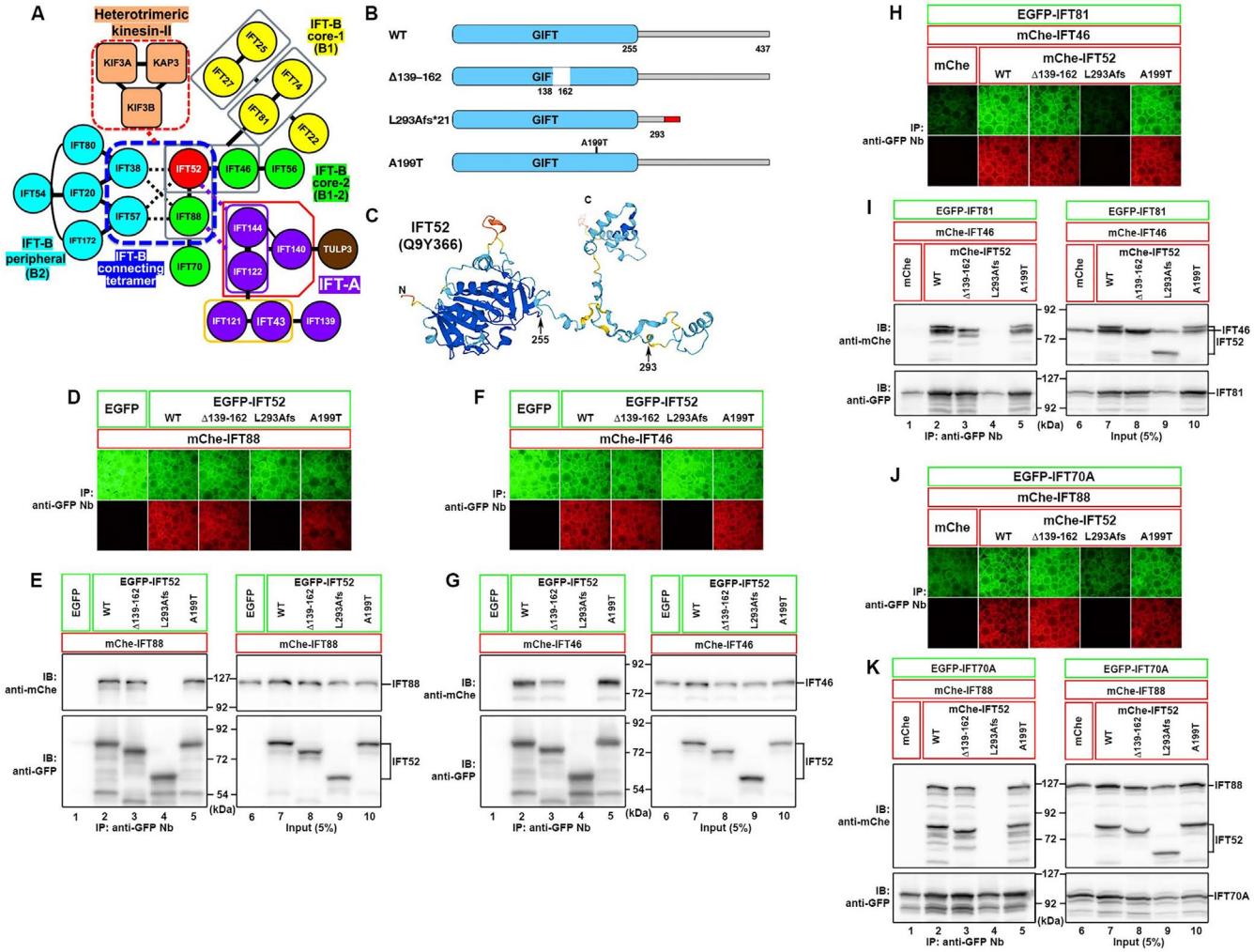

FIGURE 1: An SRPS truncation variant of IFT52 lacks the ability to interact with other IFT-B core subunits. (A) The overall architecture of the IFT- B complex and the modes of its interactions with heterotrimeric kinesin-II and the IFT-A complex predicted from our previous studies (Nakayama and Katoh, 2020). (B) The IFT52 constructs used in this study. (C) The predicted three-dimensional structure of human IFT52 in the AlphaFold Protein Structure Database (Tunyasuvunakool *et al.*, 2021). (D–G) Interactions of the SRPS variants of IFT52 with IFT88 and IFT46. Lysates prepared from HEK293T cells coexpressing EGFP-fused IFT52 constructs, as indicated, and mCherry (mChe)-IFT88 (D, E) or mCherry-IFT46 (F, G) were subjected to the VIP assay using GST-tagged anti-GFP Nb (D, F), followed by immunoblotting analysis using anti-mCherry and anti-GFP antibodies (E, G). (H–K) Interactions of the SRPS variants of IFT52 with IFT81 or IFT70A, which form a dimer with IFT46 or IFT88, respectively. Lysates of cells coexpressing EGFP-fused IFT81 (H, I) or IFT70A (J, K) and mCherry-fused IFT52 constructs, as indicated, plus mCherry-fused IFT46 (H, I) or IFT88 (J, K), were subjected to the VIP assay using GST–anti-GFP Nb (H, J), followed by immunoblotting analysis (I, K). Note that IFT81 is relatively unstable in the absence of its interacting proteins, as described previously (Katoh *et al.*, 2016; Zhou *et al.*, 2022) and that the subtle difference in the position of the IFT52 protein band in the Input and IP lanes may be due to limited degradation of the protein during the immunoprecipitation process.

Katoh *et al.*, 2016; Taschner *et al.*, 2016). On the other hand, the IFT-A complex composed of six subunits is suggested to play a major role in retrograde trafficking powered by the dynein-2 complex. In addition, the IFT-A complex contributes to membrane protein import together with the TULP3 adaptor (Anvarian *et al.*, 2019; Nakayama and Katoh, 2020).

Owing to their crucial roles, mutations in IFT components cause a class of hereditary diseases that often demonstrate multisystemic symptoms, including Bardet–Biedl syndrome (BBS) and Joubert syndrome, which are collectively referred to as the ciliopathies (Brown and Witman, 2014; Reiter and Leroux, 2017). A subset of the ciliopathies demonstrate profound abnormalities of the skeleton. These diseases include perinatally lethal short-rib polydactyly syndrome (SRPS), the less severe Jeune asphyxiating thoracic dystrophy, and the nonlethal cranioectodermal dysplasia (CED; also known as Sensenbrenner syndrome) (Schmidts, 2014; Reiter and Leroux, 2017; Zhang *et al.*, 2018). In particular, mutations in subunits of the IFT-A complex and the dynein-2 complex result in skeletal ciliopathies. We recently demonstrated the molecular mechanisms underlying ciliary defects caused by mutations in the IFT-A subunits IFT122 and IFT144 and a dynein-2 subunit, DYNC2LI1, which are found in skeletal ciliopathies (Takahara *et al.*, 2018; Ishida *et al.*, 2021; Qiu *et al.*, 2022).

On the other hand, some IFT-B subunits, including IFT52, IFT80, and IFT172, are also known to be mutated in skeletal ciliopathies (Schmidts, 2014; Zhang *et al.*, 2018; Dupont *et al.*, 2019). In this

study, we were interested in analyzing the variations in IFT52 found in CED and SRPS (Girisha *et al.*, 2016; Zhang *et al.*, 2016; Dupont *et al.*, 2019), as IFT52 is one of the hub subunits of the IFT-B complex that interacts not only with other IFT-B subunits (Taschner *et al.*, 2011; Katoh *et al.*, 2016) but also with the IFT-A complex and heterotrimeric kinesin-II (see Figure 1A) (Nakayama and Katoh, 2020); for example, 1) as described above, IFT52, together with IFT88, constitutes the interface between the IFT-B core (B1) and peripheral (B2) subcomplexes via interacting with IFT38 and IFT57 (Boldt *et al.*, 2016; Katoh *et al.*, 2016; Taschner *et al.*, 2016); 2) the IFT52/IFT88/IFT38/IFT57 tetrameric unit constitutes the binding site for heterotrimeric kinesin-II (Funabashi *et al.*, 2018); and 3) IFT52–IFT88 connects the IFT-B complex to the IFT-A complex via interacting with IFT122–IFT144 (Kobayashi *et al.*, 2021). We found that CED and SRPS variants of IFT52 are impaired in the formation of the IFT-B holocomplex from two subcomplexes and in their interaction with heterotrimeric kinesin-II, although the latter variant is more severely impaired. Furthermore, *IFT52*-knockout (KO) cells expressing IFT52 variants that mimic the cellular conditions of CED and SRPS individuals demonstrated mild defects in ciliogenesis and in anterograde ciliary protein trafficking.

RESULTS

An SRPS truncation variant of IFT52 is impaired with respect to its ability to interact with other IFT-B core subunits

To date, three families of IFT52 skeletal ciliopathies have been reported. The first case study reported a CED patient with a homozygous c.424C>T variation (Girisha *et al.*, 2016). Although the study suggested that the one-nucleotide change results in a truncated IFT52 protein, p.(Arg142*) (Girisha *et al.*, 2016), a subsequent study found that the c.424C>T variation affects splicing and results in the partial skipping of exon 6 and the production of a protein lacking 24 amino acids within the GldG intraflagellar transport (GIFT) domain, IFT52(Δ139–162) (Figure 1, B and C) (Dupont *et al.*, 2019). The second study reported SRPS individuals with the compound heterozygous variations c.878delT, p.(Leu293Alafs*21) (hereafter referred to as IFT52(L293Afs*)), and c.595G>A, p.(Ala199Thr) (Zhang *et al.*, 2016); the Ala residue within the GIFT domain is evolutionally conserved in vertebrates. The third study reported that individuals showing signs of short-rib thoracic dysplasia accompanying polydactyly have compound heterozygous *IFT52* variations (Dupont *et al.*, 2019). One variation was c.293A>G, p.(Asn98Ser), and the other consisted of the deletion of the last five nucleotides and a two-nucleotide insertion within exon 8. Although the latter variation, c.695_699delinsCA, was predicted to result in an in-frame mutation, p.(Ile232Met233delinsThr), it was shown to affect the correct splicing of exon 8, partially leading to a frameshift mutation. As there is some uncertainty regarding the protein products in the third case, we hereafter focused on the three IFT52 variants reported in the first two studies; namely, homozygous IFT52(Δ139–162) found in CED and the heterozygous IFT52(L293Afs*) and IFT52(A199T) found in SRPS (Figure 1B).

We first analyzed interactions of the IFT52 variants with other IFT-B core subunits. For this purpose, we used the visible immunoprecipitation (VIP) assay followed by immunoblotting analysis. The VIP assay is a flexible and versatile coimmunoprecipitation assay using fluorescent fusion proteins that is able to visually screen not only binary protein interactions but also one-to-many and many-to-many protein interactions. In this assay, expression vectors for enhanced green fluorescent protein (EGFP)-fused and mCherry-fused proteins are transiently cotransfected into HEK293T cells, and lysates prepared from the transfected cells are subjected to immunoprecipitation with glutathione *S*-transferase (GST)-tagged anti-GFP nanobody (Nb) prebound to Glutathione Sepharose beads. If the EGFP-fused proteins interact with the mCherry-fused proteins, not only green but also red signals can be detected on the precipitated beads under a conventional fluorescence microscope (Katoh *et al.*, 2015, 2018). However, it is important to note that the expression levels and stability of individual proteins may vary from protein to protein and be affected by the coexpressed proteins and that the interactions may also be affected by the fluorescent protein tags (Katoh *et al.*, 2015, 2016). Furthermore, as is true for many such interaction analyses using exogenous protein expression, it is not entirely guaranteed that the interactions detected actually occur under physiological conditions (within cilia in the case of this study).

In the IFT-B core subcomplex, IFT52 directly interacts with IFT46 and IFT88 (Figure 1A) (Taschner *et al.*, 2014; Katoh *et al.*, 2016). A biochemical study of *Chlamydomonas* IFT-B proteins, in conjunction with the crystallographic structure of the complex of *Tetrahymena thermophila* IFT46 and IFT52, showed that IFT52 interacts with IFT46 and IFT88 via the most C-terminal region and the middle region downstream of the GIFT domain, respectively (Taschner *et al.*, 2014). The Δ139–162 or A199T variation, each of which is located within the GIFT domain, did not substantially affect the interaction of IFT52 with IFT88 (Figure 1, D and E) or IFT46 (Figure 1, F and G), as expected from the *Chlamydomonas* study. In marked contrast, IFT52(L293Afs*) lacked the ability to interact with IFT88 (Figure 1, D and E) and IFT46 (Figure 1, F and G) (column/lane 4), meaning that the region C-terminal to the GIFT domain is involved in its interaction with IFT46 and IFT88 in this assay system.

The IFT46–IFT52 heterodimer interacts with IFT81; this interaction occurs via the connecting interface between the core-1 subgroup (IFT22/IFT25/IFT27/IFT74/IFT81) and the core-2 subgroup (IFT46/IFT52/IFT56/IFT70/IFT88) (see Figure 1A) (Katoh *et al.*, 2016). As shown in Figure 1, H and I, mCherry-fused IFT52(Δ139–162) and IFT52(A199T) as well as IFT52(wild type [WT]) were coprecipitated with EGFP-IFT81 when coexpressed with mCherry-IFT46. However, as expected from the data shown in Figure 1, F and G, mCherry-IFT46+mCherry-IFT52(L293Afs*) (hereafter, when two or more mCherry-fused proteins are coexpressed in this manner, they will be described as mCherry-IFT46+IFT52(L293Afs*)) was not coprecipitated with EGFP-IFT81 (Figure 1, H and I, column/lane 4); note that, as described previously (Katoh *et al.*, 2016; Zhou *et al.*, 2022), IFT81 alone is relatively unstable in the absence of its interacting proteins (Figure 1I, columns/lanes 6 and 9 in the bottom panel).

There are two IFT70 isoforms in humans. IFT70B interacts with the IFT52–IFT88 dimer, whereas IFT70A interacts with the IFT52–IFT88 dimer and with IFT52 alone at a lower efficiency (Takei *et al.*, 2018). As shown in Figure 1, J and K, IFT52(Δ139–162)+IFT88 and IFT52(A199T)+IFT88 were coprecipitated with IFT70A at a level comparable to that of IFT52(WT)+IFT88. By contrast, IFT52(L293Afs*)+IFT88 was not coprecipitated with IFT70A (Figure 1, J and K, column/lane 4). The results shown in Figure 1, J and K, are consistent with a previous biochemical study showing that *Chlamydomonas* IFT70 interacts with the middle region of IFT52 (Taschner *et al.*, 2011).

GIFT-domain variants as well as a truncation variant of IFT52 are compromised regarding the formation of the connecting tetramer and interaction with heterotrimeric kinesin-II

IFT52 participates in composite interactions required for the connection of the two IFT-B subcomplexes; namely, formation of the connecting tetramer composed of IFT52+IFT88 from the core (IFT-B1) subcomplex and IFT38+IFT57 from the peripheral (IFT-B2)

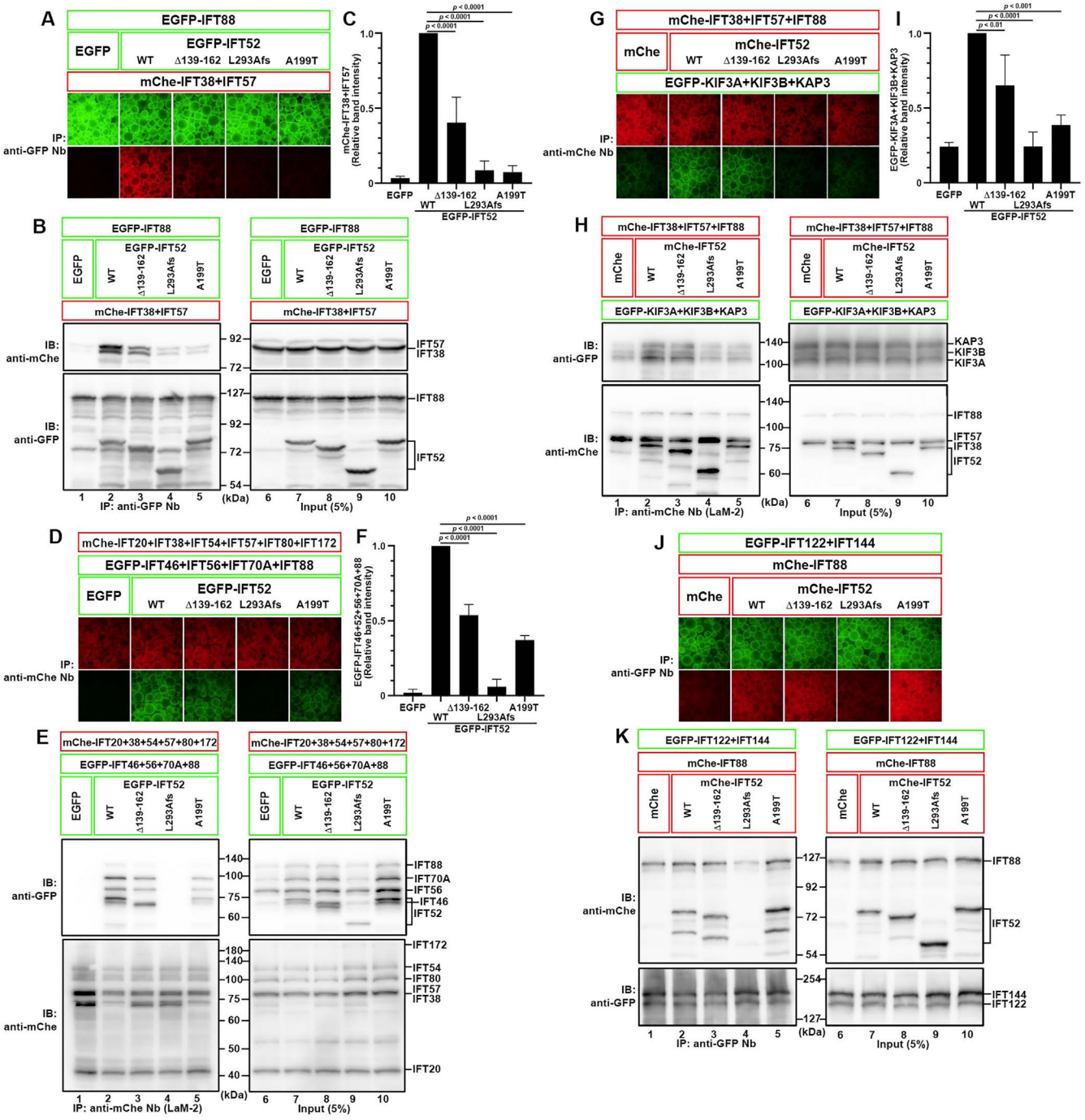

FIGURE 2: GIFT-domain variants as well as a truncation variant of IFT52 are compromised regarding the formation of the connecting tetramer and interaction with heterotrimeric kinesin-II. (A, B) Abilities of the IFT52 variants to form the connecting tetramer together with IFT38, IFT57, and IFT88. Lysates of cells coexpressing EGFP-IFT88, the EGFP-fused IFT52 constructs, as indicated, and mCherry (mChe)-fused IFT38+IFT57 were subjected to the VIP assay using GST–anti-GFP-Nb (A), followed by immunoblotting analysis using anti-mChe and anti-GFP antibodies (B). Note that the fact that the IFT38 and IFT57 bands appear in different positions in the IP lanes may be due to limited degradation of either protein. (C) The band intensities of mChe-IFT38+IFT57 coimmunoprecipitated with anti-GFP Nb in B were measured using ImageJ software, and the relative band intensities with the total band intensity of lane 2 taken as 1.0 are shown as bar graphs. The values are means ± SD of three independent experiments. Statistical significances were calculated using one-way analysis of variance (ANOVA) followed by the Dunnett multiple comparison test. (D, E) Abilities of the IFT52 variants to constitute the interface between the IFT-B core and peripheral subcomplexes. Lysates of cells coexpressing EGFP-fused IFT52 constructs, as indicated, plus EGFP-fused IFT46+IFT56+IFT70A+IFT88 and mChe-fused IFT-B peripheral subunits were subjected to the VIP assay using GST–anti-mChe Nb (the LaM-2 version) (D), followed by immunoblotting analysis using anti-GFP and anti-mChe antibodies (E). (F) The band intensities of EGFP-fused IFT52 constructs plus EGFP-IFT46+IFT56+IFT70A+IFT88 coimmunoprecipitated with anti-mChe Nb in E were analyzed as described in C. (G, H) Abilities of the IFT52 variants to interact with heterotrimeric kinesin-II together with

subcomplex (Figure 1A) (Katoh *et al.*, 2016; Taschner *et al.*, 2016). When coexpressed with EGFP-IFT88, EGFP-fused IFT52(A199T) as well as IFT52(L293Afs*) was substantially impaired with respect to its interaction with mCherry-fused IFT38+IFT57, compared with IFT52(WT) (Figure 2, A and B, compare columns/lanes 4 and 5 with column/lane 2; also see Figure 2C). In addition, IFT52(Δ139–162) appeared to be partially compromised regarding tetramer formation (Figure 2, A and B, compare column/lane 3 with column/lane 2). We then analyzed the interaction between mCherry-fused peripheral (IFT-B2) subunits (IFT20+IFT38+IFT54+IFT57+IFT80+IFT172) and EGFP-fused core-2 subgroup subunits (IFT46+IFT56+IFT70A+IFT88) containing IFT52(WT) or one of the skeletal ciliopathy variants (Figure 2, D–F); note that the expression level of mCherry-IFT172 was relatively low due to its large size (Figure 2E, bottom right panel). The core-2 subgroup containing IFT52(L293Afs*) completely lost the ability to interact with the peripheral subcomplex (Figure 2, D and E, compare column/lane 4 with column/lane 2). The IFT52(A199T)-containing core-2 subgroup demonstrated a partially reduced ability to interact with the peripheral subcomplex (Figure 2, D and E, column/lane 5; also see Figure 2F). The core-2 subgroup containing IFT52(Δ139–162) appeared to be slightly affected in its interaction with the peripheral subcomplex (Figure 2, D and E, column/lane 3). Thus, results of the interactions of the core-2 subgroup containing the IFT52 variant with the peripheral subcomplex (Figure 2, D–F) are largely consistent with the results of the interactions of the IFT88+IFT52 variant with IFT38+IFT57 (Figure 2, A–C). However, IFT52(A199T) in the core-2 subgroup appeared to be less affected compared with IFT52(A199T)+IFT88 (compare lane 5 with lane 2 in Figure 2, B and E); this is probably because the presence of multiple core-2 subunits compensated for the reduced ability of IFT52(A199T) to interact with the peripheral subunits.

We previously showed that the connecting tetramer IFT38/IFT52/IFT57/IFT88 constitutes the binding site for heterotrimeric kinesin-II and found that absence of the interaction between the tetramer and kinesin-II results in a severe ciliogenesis defect, indicating that docking of kinesin-II to the IFT-B complex is a prerequisite for the anterograde transport of the IFT machinery (Funabashi *et al.*, 2018). In agreement with this previous study, the EGFP-fused kinesin-II subunits KIF3A+KIF3B+KAP3 were coimmunoprecipitated with mCherry-fused IFT38+IFT52(WT)+IFT57+IFT88 (Figure 2, G and H, column/lane 2). However, when mCherry-fused IFT52(L293Afs*) or IFT52(A199T) was used in place of IFT52(WT), the amounts of the coprecipitated EGFP-fused kinesin-II subunits were reduced to the amount in the absence of IFT52 (Figure 2, G and H, compare columns/lanes 4 and 5 with column/lane 1; also see Figure 2I), suggesting that the interaction of kinesin-II with the IFT-B complex containing IFT52(L293Afs*) or IFT52(A199T) is substantially impaired. The IFT52(Δ139–162) variation appeared to marginally affect the interaction of the connecting tetramer with heterotrimeric kinesin-II (Figure 2, G and H, column/lane 3; also see Figure 2I).

We recently showed that IFT52–IFT88 from the IFT-B complex and IFT122–IFT144 from the IFT-A complex constitute the interface between the two complexes and found that the IFT-A–IFT-B interaction is required for ciliary retrograde protein trafficking and import of G protein–coupled receptors (GPCRs) into cilia (Kobayashi *et al.*, 2021). As shown in Figure 2, J and K, when coexpressed with mCherry-IFT88, mCherry-fused IFT52(L293Afs*) was not coprecipitated with EGFP-IFT122+IFT144 (column/lane 4), whereas IFT52(Δ139–162) and IFT52(A199T) were coprecipitated with IFT122+IFT144 at a level comparable to that of IFT52(WT) (compare columns/lanes 3 and 5 with column/lane 2).

Taking the data shown in Figures 1 and 2 together, we conclude that IFT52(L293Afs*) is a null mutant regarding its interactions with other IFT-B subunits. IFT52(A199T) is impaired with respect to the formation of the IFT-B connecting tetramer and the interaction of the tetramer with heterotrimeric kinesin-II, whereas the IFT52(Δ139–162) variation has only a minor effect on connecting tetramer formation.

GIFT-domain variations of IFT52 have moderate effects on cilia biogenesis and ciliary localization of IFT-B

We then established *IFT52*-KO cells from human telomerase reverse transcriptase–immortalized retinal pigment epithelial 1 (hTERT-RPE1) cells using the CRISPR/Cas9 system (Supplemental Figure S1, A–D). Similar to the KO of other IFT-B core subunits in RPE1 cells (Katoh *et al.*, 2017; Nakayama and Katoh, 2018; Takei *et al.*, 2018; Zhou *et al.*, 2022), the *IFT52*-KO cell lines established using distinct target sequences (#IFT52-2-8 and #IFT52-3-12) completely lacked cilia (Supplemental Figure S1, E–G) and IFT88 signals at the basal body (Supplemental Figure S1, H–J), indicating that the functional IFT-B complex is not assembled in the absence of IFT52. Stable expression of mCherry-fused IFT52(WT), but not mCherry alone, using a lentiviral vector in *IFT52*-KO cells (#IFT52-2-8) rescued the ciliogenesis defects (Figure 3, A and B); the ciliogenesis efficiency of *IFT52*-KO cells expressing IFT52(WT) was not significantly different from that of control RPE1 cells (Supplemental Figure S3, A–D). As expected from the interaction experiments (Figures 1 and 2), expression of mCherry-IFT52(L293Afs*) in *IFT52*-KO cells did not restore cilia formation at all (Figure 3D), indicating that IFT52(L293Afs*) is functionally null. By contrast, stable expression of mCherry-IFT52(Δ139–162) or mCherry-IFT52(A199T) substantially restored cilia formation (Figure 3, C and E), although the ciliogenesis efficiency was significantly lower in IFT52(Δ139–162)- or IFT52(A199T)-expressing cells than in IFT52(WT)-expressing cells (see Figure 4I); the mild ciliogenesis defect of *IFT52*-KO cells expressing IFT52(Δ139–162) or IFT52(A199T) is in line with previous analyses of fibroblasts derived from CED and SRPS individuals (Zhang *et al.*, 2016; Dupont *et al.*, 2019).

We also noticed another difference between *IFT52*-KO cells expressing IFT52(WT) and those expressing IFT52(Δ139–162) or IFT52(A199T). The ciliary length was more variable in cells expressing IFT52(Δ139–162) or IFT52(A199T) than in those expressing IFT52(WT), although we could not detect a significant difference in mean ciliary length between them (see Figure 4J); we confirmed that the ciliary length variability of IFT52(WT)-expressing *IFT52*-KO cells was not significantly different from that of control RPE1 cells

IFT38, IFT57, and IFT88. Lysates of cells coexpressing mChe-fused IFT52 constructs, as indicated, mChe-fused IFT38+IFT57+IFT88, and EGFP-fused KIF3A+KIF3B+KAP3 were subjected to the VIP assay using GST–anti-mChe Nb (the LaM-2 version) (G), followed by immunoblotting analysis using anti-GFP and anti-mChe antibodies (H). (I) The band intensities of EGFP-KIF3A+KIF3B+KAP3 coimmunoprecipitated with anti-mChe Nb in H were analyzed as described in C. (J, K) Abilities of the IFT52 variants to constitute the interface between the IFT-A and IFT-B complexes. Lysates of cells coexpressing mChe-fused IFT52 constructs, as indicated, mChe-IFT88, and EGFP-fused IFT122+IFT144 were subjected to the VIP assay using GST–anti-GFP Nb (J), followed by immunoblotting analysis using anti-mChe and anti-GFP antibodies (K).

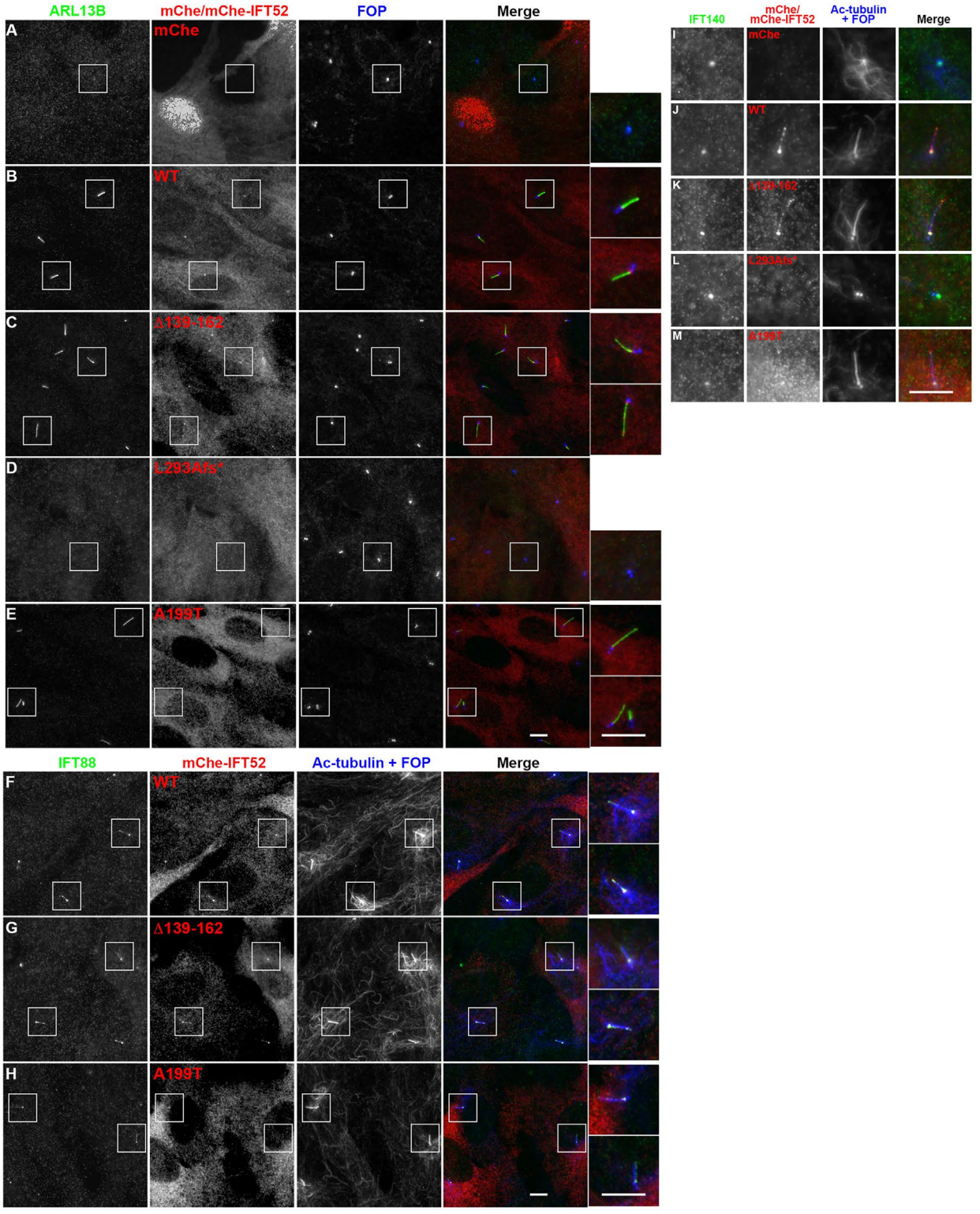

FIGURE 3: GIFT-domain variations of IFT52 have moderate effects on cilia biogenesis and IFT-B ciliary localization. (A–E) *IFT52*-KO cells expressing mCherry (mChe) (A) or mChe-fused IFT52(WT) (B), IFT52(Δ139–162) (C), IFT52(L293Afs*) (D), or IFT52(A199T) (E) were serum-deprived for 24 h and immunostained with antibodies against ARL13B, RFP (which recognizes mChe), and FOP (recently renamed as CEP43). (F–H) *IFT52*-KO cells expressing mChe-fused IFT52(WT) (F), IFT52(Δ139–162) (G), or IFT52(A199T) (H) were serum-deprived for 24 h and immunostained with antibodies against IFT88, RFP, and Ac-tubulin + FOP. The right panels are 2.5-fold-enlarged images of the boxed regions. (I–M) *IFT52*-KO cells expressing mChe (I) or mChe-fused IFT52(WT) (J), IFT52(Δ139–162) (K), IFT52(L293Afs*) (L), or IFT52(A199T) (M) were serum-deprived for 24 h and immunostained with antibodies against IFT140, RFP, and Ac-tubulin + FOP. Scale bars, 5 μm. Note that the results of statistical analyses of cilia formation, ciliary length variation, and IFT88 ciliary staining intensity are shown in Figure 4, I–K, combined with those of Figure 4, A–H.

(Supplemental Figure S3E). The ciliary length variability as well as the difference in the ciliogenesis efficiency suggests that the GIFT-domain variants IFT52(Δ139–162) and IFT52(A199T) are not equivalent to IFT52(WT) in terms of cilia biogenesis, although it cannot be strictly ruled out that the length variability may reflect the variability in the expression level of the IFT52 protein in individual cells.

We then analyzed the localization of IFT88 in *IFT52*-KO cells expressing IFT52(WT), IFT52(Δ139–162), or IFT52(A199T). In *IFT52*-KO cells expressing mCherry-IFT52(WT), IFT88 was mainly found at the ciliary base, with a minor proportion at the tip (Figure 3F), as in control RPE1 cells (Supplemental Figure S1H). These IFT88 signals were also observed in *IFT52*-KO cells expressing mCherry-IFT52(Δ139–162) or mCherry-IFT52(A199T) (Figure 3, G and H). However, we noticed that IFT52(A199T)-expressing cells had a tendency to have IFT88 signals less intense than those of IFT52(WT)-expressing cells; the ciliary IFT88 signal intensity of *IFT52*-KO cells expressing IFT52(WT) was not significantly different from that of control RPE1 cells (Supplemental Figure S3, F–I). Statistical analysis of the IFT88 staining intensity in whole cilia (ciliary base, shaft, and tip) confirmed that the intensity was significantly lower in IFT52(A199T)-expressing *IFT52*-KO cells than in IFT52(WT)-expressing cells (see Figure 4K). In IFT52(Δ139–162)-expressing *IFT52*-KO cells, the IFT88 staining intensity also tended to be lower than in IFT52(WT)-expressing cells, but the difference was not statistically significant (Figure 4K).

We also analyzed the localization of IFT140, an IFT-A subunit. IFT140 signals were found predominantly at the ciliary base not only in *IFT52*-KO cells expressing mCherry-IFT52(WT) (Figure 3J) but also in those expressing mCherry alone (Figure 3I) or any of the IFT52 variants (Figure 3, K–M); the IFT140 localization in *IFT52*-KO cells expressing IFT52(WT) was confirmed to be similar to that in control RPE1 cells (Supplemental Figure S3, J–L). These observations suggest that the IFT-A complex can be recruited to the ciliary base independently of the IFT-B complex.

Two ciliary GPCRs are known to participate in Hh signaling. Under basal conditions, GPR161 on the ciliary membrane represses Hh signaling. When the Hh pathway is activated, Smoothened (SMO) enters and GPR161 exits cilia, resulting in the derepression of Hh signaling. In *IFT52*-KO cells expressing mCherry-IFT52(WT), GPR161 was present within cilia (Supplemental Figure S2A) and SMO was absent from cilia (Supplemental Figure S2K) under basal conditions. When these cells were treated with Smoothened Agonist (SAG), the ciliary GPR161 level was decreased (Supplemental Figure S2F; also see Supplemental Figure S2U), whereas the SMO level within cilia was increased (Supplemental Figure S2P; also see Supplemental Figure S2V). Somewhat unexpectedly, changes in the ciliary levels of GPR161 (Supplemental Figure S2, B, C, G, and H; also see Supplemental Figure S2U) and SMO (Supplemental Figure S2, L, M, Q, and R; also see Supplemental Figure S2V) by SAG treatment in IFT52(Δ139–162)-expressing and IFT52(A199T)-expressing *IFT52*-KO cells were essentially the same as in IFT52(WT)-expressing cells.

Cellular conditions mimicking heterozygous IFT52 variations in SRPS cause moderate defects in ciliogenesis and ciliary IFT-B localization

We then analyzed the effects of expression of the combination of IFT52(A199T) and IFT52(L293Afs*) in *IFT52*-KO cells, which mimics the cellular conditions of SRPS individuals (Zhang *et al.*, 2016). As described above, *IFT52*-KO cells expressing mCherry-IFT52(A199T) demonstrated mild ciliogenesis defects and had a more diverse ciliary length distribution than those expressing mCherry-IFT52(WT) (Figure 4, A and B; also see Figure 4, I and J). When mCherry-IFT52(L293Afs*) was coexpressed together with mCherry-IFT52(WT) in *IFT52*-KO cells, which mimics the cellular conditions of a healthy parent of SRPS individuals, the ciliogenesis efficiency was comparable to that of *IFT52*-KO cells expressing mCherry-IFT52(WT) alone (Figure 4, C and I), although the ciliary length tended to vary slightly (Figure 4J). However, when mCherry-IFT52(L293Afs*) was coexpressed with mCherry-IFT52(A199T) in *IFT52*-KO cells, similarly to those expressing IFT52(A199T) alone, ciliogenesis was moderately compromised compared with those expressing IFT52(WT)+IFT52(L293Afs*) (Figure 4, D and I). The variation in ciliary length was greater in *IFT52*-KO cells expressing IFT52(A199T)+IFT52(L293Afs*) or IFT52(A199T) alone than in those expressing IFT52(WT) (Figure 4J). In this context, it is worth noting that SRPS fibroblasts were reported to have cilia with a more diverse length distribution than cilia of control fibroblasts (Zhang *et al.*, 2016).

Measurement of the ciliary IFT88 staining intensity (Figure 4K) demonstrated that the intensity was significantly lower in *IFT52*-KO cells expressing IFT52(A199T) alone or IFT52(A199T)+IFT52(L293Afs*) (Figure 4, F and H) than in IFT52(WT)-expressing and IFT52(WT)+IFT52(L293Afs*)-expressing cells (Figure 4, E and G). These observations, together with the interaction data (Figures 1 and 2), suggest that IFT52(L293Afs*) is a functionally null variant and that the mild ciliary defects in *IFT52*-KO cells expressing IFT52(A199T)+IFT52(L293Afs*) are attributable to the IFT52(A199T) variant alone.

We then analyzed whether IFT52(A199T) expression in *IFT52*-KO cells affects the stability of the IFT-B components. The levels of IFT88 and IFT70 in lysates prepared from *IFT52*-KO cells were considerably decreased compared with those from control RPE1 cells (Figure 4L, compare lane 2 with lane 1), indicating that the IFT-B components are unstable in the absence of IFT52. Expression of IFT52(WT)+IFT52(L293Afs*) or IFT52(A199T)+IFT52(L293Afs*) substantially increased IFT88 and IFT70 levels toward, although not equivalent to, those in control cells (Figure 4L, lanes 3 and 4). In view of the fact that the SRPS variants of IFT52 are impaired with respect to constituting the interface between the core and peripheral subcomplexes and the binding site for heterotrimeric kinesin-II (Figure 2), the data shown in Figure 4, K and L, suggest that the decrease in the ciliary IFT88 staining intensity in IFT52(A199T)-expressing and IFT52(A199T)+IFT52(L293Afs*)-expressing *IFT52*-KO cells is not simply due to a decrease in the total cellular amount of the IFT-B complex, but rather is due to a decrease in incorporation of the IFT-B complex into the anterograde IFT train at the ciliary base or in its kinesin-II–driven entry into cilia.

We also analyzed changes in the levels of GPR161 (Supplemental Figure S2, D, E, I, and J) and SMO (Supplemental Figure S2, N, O, S, and T) in response to SAG treatment in *IFT52*-KO cells expressing IFT52(WT)+IFT52(L293Afs*) or IFT52(A199T)+IFT52(L293Afs*) and confirmed that these changes are similar to each other and to those expressing IFT52(WT) or IFT52(A199T) alone (Supplemental Figure S2, U and V).

Anterograde protein trafficking toward the ciliary tip is compromised in cells expressing GIFT-domain variants of IFT52

The decrease in the ciliary level of the IFT-B complex or in its entry into cilia suggests the possibility that anterograde trafficking of ciliary proteins is compromised in *IFT52*-KO cells expressing the IFT52 variant. To address this possibility, we utilized KIF17, homodimeric kinesin-2 found at the ciliary tip, and ICK/CILK1, a MAPK-like kinase regulating the turnaround event of the IFT machinery at the tip

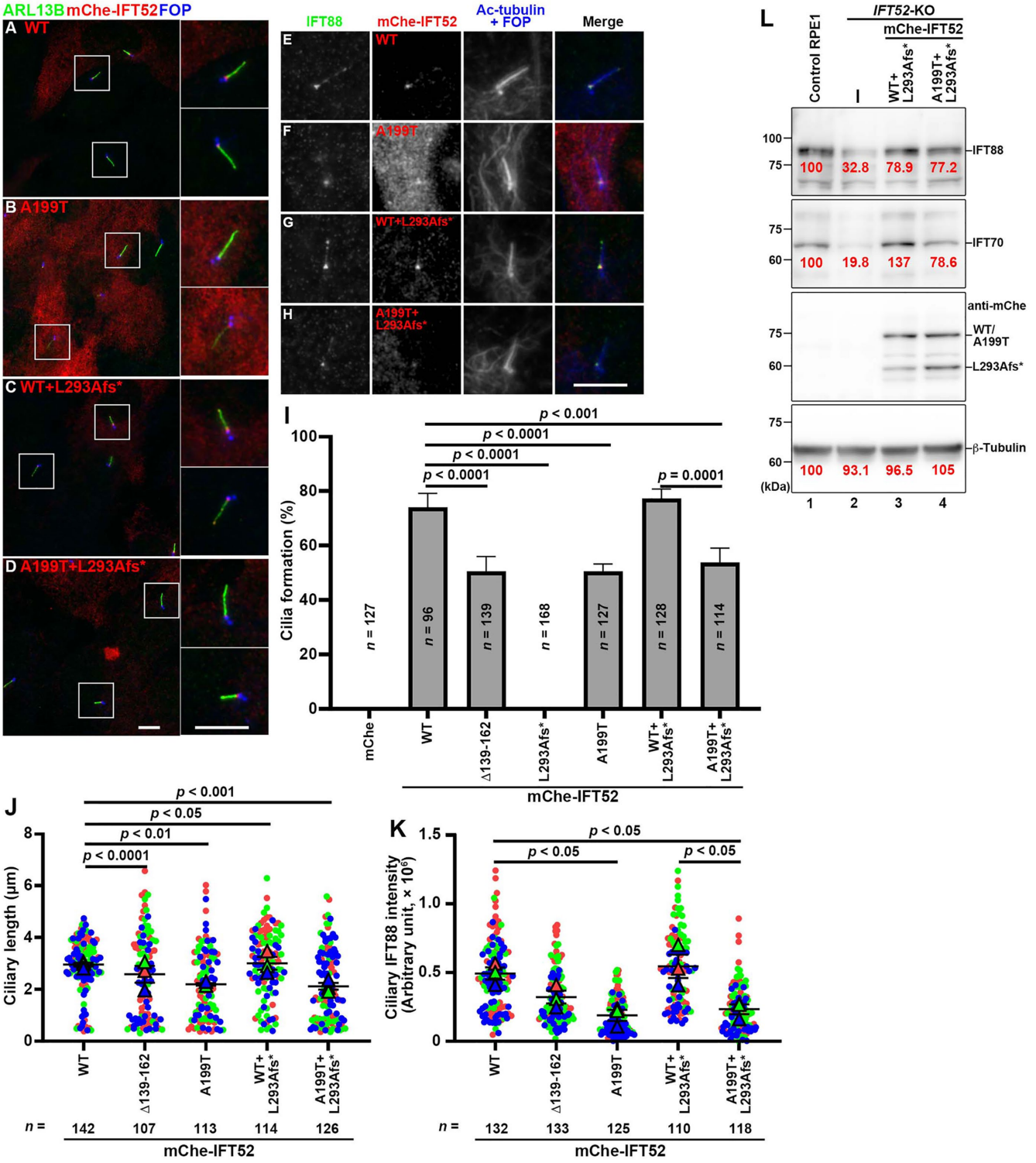

FIGURE 4: Cells mimicking the conditions of SRPS with IFT52 variations demonstrate moderate defects in ciliogenesis and IFT-B localization. (A–H) *IFT52*-KO cells expressing mCherry (mChe)-fused IFT52(WT) (A, E), IFT52(A199T) (B, F), IFT52(WT)+IFT52(L293Afs*) (C, G), or IFT52(A199T)+IFT52(L293Afs*) (D, H) were analyzed as described in the legend for Figure 3, A–E and F–H. Scale bars, 5 μm. (I) Ciliated cells in the experiments shown in Figure 3, A–E, and A–D here were counted, and percentages of ciliated cells are expressed as bar graphs. Values are means ± SD of three independent experiments; note that sets of experiments shown in Figure 3, A–E, and A–D here were carried out on the same days. In each set of experiments, 31–70 cells were analyzed, and the total numbers of analyzed cells are shown (*n*). Statistical significances were calculated using the Fisher exact test. (J) Ciliary lengths of individual ciliated cells were measured and are expressed as scatter plots. Differently colored dots represent three independent experiments, and triangles and horizontal lines indicate means and SD, respectively. In each set of experiments, 31–58 cells were analyzed, and the total numbers of analyzed cells are shown (*n*). Statistical significances in the variation of ciliary lengths of individual

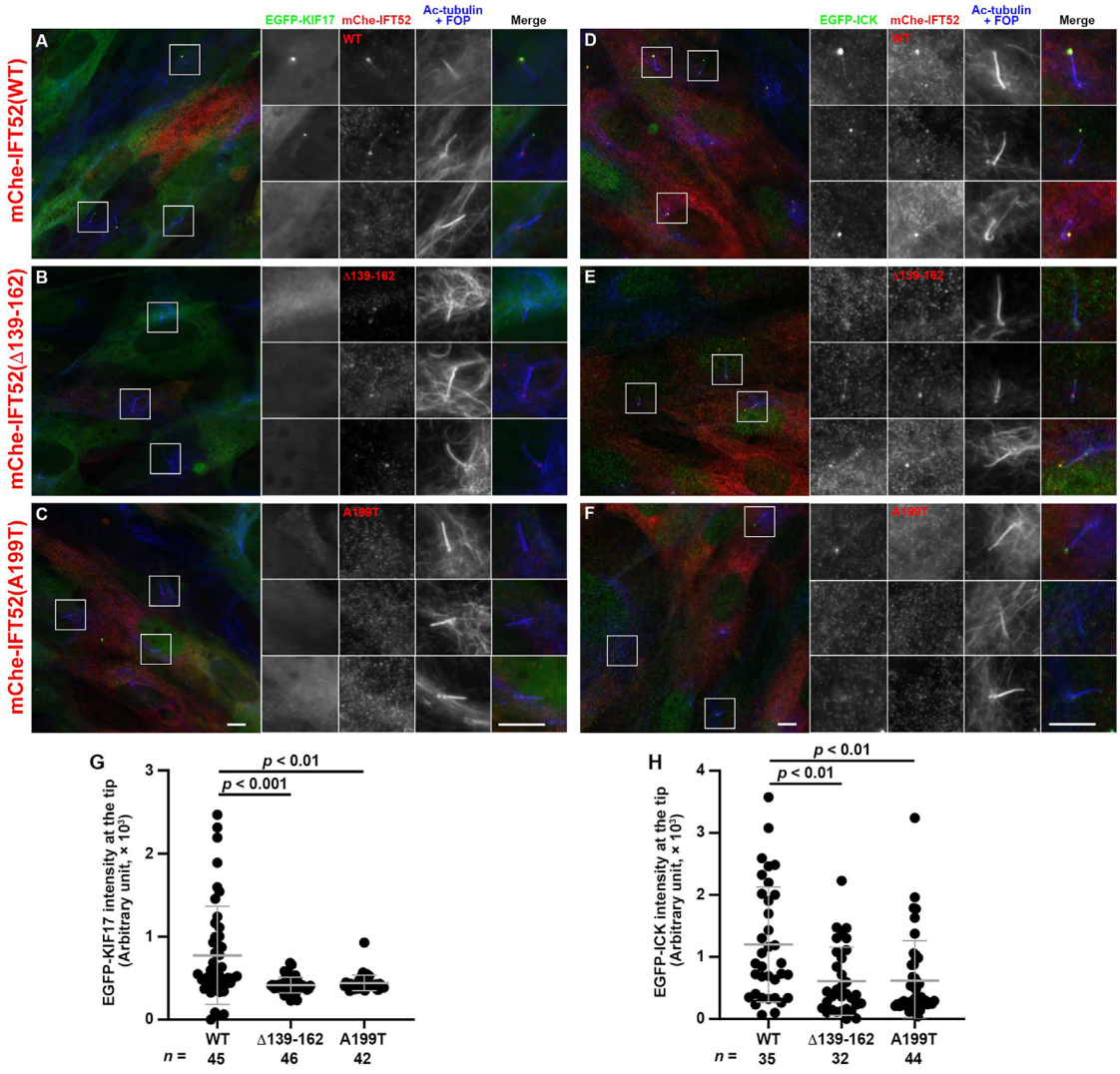

FIGURE 5: Impaired tip localization of KIF17 and ICK in *IFT52*-KO cells expressing IFT52(Δ139–162) or IFT52(A199T). (A–F) *IFT52*-KO cells stably expressing mCherry (mChe)-fused IFT52(WT) (A, D), IFT52(Δ139–162) (B, E), or IFT52(A199T) (C, F) were infected with a lentiviral vector for EGFP-fused KIF17 (A–C) or ICK (D–F), and cells stably expressing these proteins were selected. The cells were then serum-deprived for 24 h and immunostained with antibodies against RFP, Ac-tubulin, and FOP (A–C) or those against GFP, RFP, Ac-tubulin, and FOP (D–F). Scale bars, 5 μm. (G, H) The signal intensities of EGFP-KIF17 (G) and EGFP-ICK (H) at the ciliary tips were measured and are expressed as scatter plots. Horizontal lines and error bars indicate means and SD, respectively. Total numbers of analyzed cells are shown (*n*). Statistical significances were calculated using one-way ANOVA followed by the Dunnett multiple comparison test.

(Funabashi *et al.*, 2017; Nakamura *et al.*, 2020); although our recent study suggested that KIF17 is transported to the tip via binding to the IFT-B complex in hTERT-RPE1 cells (Funabashi *et al.*, 2017), it is also possible that KIF17 drives anterograde trafficking of the IFT machinery as in the case of *C. elegans* sensory cilia (Prevo *et al.*, 2017). When EGFP-KIF17 was expressed in *IFT52*-KO cells expressing mCherry-IFT52(WT), it demonstrated a distinct localization at the ciliary tip (Figure 5A), as described previously in control RPE1 cells (Funabashi *et al.*, 2017). In *IFT52*-KO cells expressing mCherry-IFT52(Δ139–162), however, the tip localization of EGFP-KIF17 was abolished (Figure 5B). Similarly, EGFP-KIF17 was not detectable at the tip in mCherry-IFT52(A199T)–expressing *IFT52*-KO cells (Figure 5C; also see Figure 5G). In the case of EGFP-ICK, it was found mainly at the ciliary tip and at the base in *IFT52*-KO cells expressing

cells were calculated using the *F* test. (K) The IFT88 staining intensities in whole cilia of individual cells were measured and are expressed as scatter plots. Differently colored dots represent three independent experiments, and triangles and horizontal lines indicate means and SD, respectively. In each set of experiments, 32–59 cells were analyzed, and total numbers of analyzed cells are shown (*n*). Statistical significances were calculated using one-way ANOVA followed by the Tukey multiple comparison test. (L) Lysates of control RPE1 cells (lane 1), *IFT52*-KO cells (lane 2), those expressing mChe-fused IFT52(WT)+IFT52(L293Afs*) (lane 3), and those expressing mChe-fused IFT52(A199T)+IFT52(L293Afs*) were subjected to SDS–PAGE followed by immunoblotting analysis using antibodies against IFT88, IFT70, mChe, and β-tubulin. Relative band intensities are shown with the band intensity of lane 1 taken as 100%.

mCherry-IFT52(WT) (Figure 5D), as described previously in control RPE1 cells (Nakamura *et al.*, 2020; Noguchi *et al.*, 2021; Satoda *et al.*, 2022). By contrast, the level of EGFP-ICK at the tip was significantly reduced in *IFT52*-KO cells expressing mCherry-fused IFT52(Δ139–162) or IFT52(A199T) (Figure 5, E and F; also see Figure 5H). Given that KIF17 and ICK are transported via binding to the IFT-B complex (Funabashi *et al.*, 2017; Nakamura *et al.*, 2020), these observations indicate that their anterograde trafficking mediated by the IFT machinery is impaired in *IFT52*-KO cells expressing the GIFT-domain missense variant, IFT52(A199T). It is also possible that the IFT52 mutation affected the binding of KIF17 and ICK to the IFT machinery. However, at least in the case of KIF17, this possibility is unlikely because KIF17 binds the IFT-B complex via IFT46–IFT56 and not via IFT52 (Funabashi *et al.*, 2017). In the case of ICK, it interacts with the IFT-B complex via both the core (IFT-B1) and peripheral (IFT-B2) subcomplexes (Nakamura *et al.*, 2020).

DISCUSSION

Mutations in subunits of the IFT-A and dynein-2 complexes are known to cause skeletal ciliopathies (Schmidts, 2014; Schmidts *et al.*, 2015; McInerney-Leo *et al.*, 2015; Zhang *et al.*, 2018), and we recently clarified the molecular basis underlying these ciliopathies caused by mutations in the IFT-A and dynein-2 subunits (IFT122, IFT144, and DYNC2LI1) (Takahara *et al.*, 2018; Ishida *et al.*, 2021; Qiu *et al.*, 2022). In the present study, we investigated the molecular and ciliary defects caused by skeletal ciliopathy-associated mutations of IFT52, which is a subunit of the IFT-B complex and constitutes, together with other subunits, the binding site for heterotrimeric kinesin-II. IFT52(Δ139–162), a variation that was found in a homozygous CED patient (Girisha *et al.*, 2016; Dupont *et al.*, 2019), demonstrated mild defects in the formation of the IFT-B holocomplex from two subcomplexes (Figure 2). In the two variations, IFT52(L293Afs*) and IFT52(A199T), found in compound heterozygous SRPS individuals (Zhang *et al.*, 2016), the former variant was virtually incapable of forming the IFT-B holocomplex along with the other subunits (Figures 1 and 2) and was functionally null (Figure 3). The other SRPS variant, IFT52(A199T), demonstrated moderate defects in IFT-B holocomplex formation and a severe defect with respect to the interaction of the IFT-B complex with heterotrimeric kinesin-II (Figure 2).

IFT52-KO cells expressing IFT52(Δ139–162) demonstrated mild defects in cilia biogenesis (Figures 3C and 4, I and J) and had a tendency of a reduction in ciliary IFT88 level (Figures 3G and 4K). On the other hand, *IFT52*-KO cells expressing IFT52(A199T) alone or in combination with IFT52(L293Afs*) demonstrated a significantly reduced level of ciliary IFT88 (Figure 4, E–H and K) in addition to mild ciliogenesis defects (Figure 4, A–D, I, and J). As IFT52(L293Afs*) is a functionally null variant, IFT52(A199T) is likely to be responsible for the abnormal phenotype of cells expressing IFT52(A199T)+IFT52(L293Afs*). In view of the interaction data showing that IFT52(Δ139–162) and IFT52(A199T) have reduced abilities to contribute to the formation of the IFT-B holocomplex from the two subcomplexes (Figure 2, A–F) and to the interaction of the IFT-B complex with heterotrimeric kinesin-II (Figure 2, G–I), although the degree of reduction was greater for IFT52(A199T) than for IFT52(Δ139–162), these observations suggest that anterograde trafficking of the IFT machinery driven by kinesin-II is compromised in *IFT52*-KO cells expressing the IFT52 variants. These subtle differences between the variants in protein–protein interactions may be reflected in the difference in severity of ciliopathies (SRPS, perinatally lethal; CED, nonlethal).

In line with this, the ciliary tip localization of ICK and KIF17, both of which are suggested to be transported to the tip via binding to the IFT-B complex (Funabashi *et al.*, 2017; Nakamura *et al.*, 2020), was significantly reduced in *IFT52*-KO cells expressing IFT52(Δ139–162) or IFT52(A199T) compared with those expressing IFT52(WT) (Figure 5). Thus, it is likely that the developmental abnormalities of the CED patient with homozygous IFT52(Δ139–162) (Girisha *et al.*, 2016; Dupont *et al.*, 2019) and of the SRPS individuals with compound heterozygous IFT52(A199T) and IFT52(L293Afs*) variations (Zhang *et al.*, 2016) are attributable, at least in part, to defects in anterograde ciliary protein trafficking. Although the data presented in this study did not clearly explain the differences in severity of the ciliopathies, namely, between the prenatal/perinatal lethality of SRPS individuals and the survival to adulthood of CED patients, subtle phenotypic differences at the cellular level may lead to differences in skeletal development at the level of the individual.

Among the IFT-B subunits, IFT52 is a component of the core-2 (B1-2) subgroup of the core subcomplex (see Figure 1A). On the other hand, we recently clarified the molecular basis of BBS-associated ciliary defects caused by variations of IFT27/BBS19 and IFT74/BBS22 (Zhou *et al.*, 2022), which are both components of the core-1 (B1-1) subgroup (see Figure 1A). The IFT25–IFT27 dimer constitutes the interface of the IFT-B complex with the BBSome (Eguether *et al.*, 2014; Liew *et al.*, 2014) and interacts with the IFT74–IFT81 dimer in the core-1 subgroup (Taschner *et al.*, 2011; Katoh *et al.*, 2016), and hence variations of IFT27 and IFT74 likely affect the interaction of the IFT-B complex with the BBSome (Zhou *et al.*, 2022). Thus, even in the same IFT-B core (IFT-B1) subcomplex, different subunits play distinct roles via interacting with distinct proteins, and variations of distinct subunits lead to distinct abnormal phenotypes via distinct ciliary defects.

Among the IFT-B subunits, IFT80 and IFT172 are also known to be mutated in the skeletal ciliopathies (Schmidts, 2014; Zhang *et al.*, 2018); both IFT80 and IFT172 are included in the peripheral IFT-B (IFT-B2) subcomplex (see Figure 1A). Thus, the mechanism by which variations of IFT80 and IFT172 cause skeletal ciliopathies is expected to be different from the mechanism by which IFT52 variations cause them. On the other hand, mutations of IFT172/BBS20 are also known to cause BBS (Bujakowska *et al.*, 2015; Schaefer *et al.*, 2016; Hirano *et al.*, 2020). Thus, it is likely that distinct variations even in the same IFT-B subunit result in distinct ciliary defects, probably via affecting distinct protein–protein interactions. The approach used in this study, namely, linking abnormalities in protein–protein interactions caused by genetic variations to cellular defects, will be useful in elucidating differences in the pathogenesis of the ciliopathies.

Regarding the mild ciliogenesis defects, *IFT52*-KO cells expressing IFT52(Δ139–162) or IFT52(A199T)+IFT52(L293Afs*) phenocopy fibroblasts derived from patients with CED and SRPS (Zhang *et al.*, 2016; Dupont *et al.*, 2019). Thus, the phenotype of *IFT52*-KO cells expressing the IFT52 protein with a variation observed in patients can, at least to some extent, reflect the phenotype of the patient-derived cells. In view of the facts that primary cultured cells derived from patients are often difficult to culture for long periods of time and that they are available to only a limited number of researchers, our approach of genome editing immortalized normal human cultured cells and then mimicking the ciliopathy genotype is useful. However, in our experimental system, we use a recombinant virus to express the variant gene in KO cells, and hence the level of the expressed protein cannot be strictly controlled. In the future, the introduction of variations into endogenous genes using genome-editing technologies, such as base editing (Porto *et al.*, 2020), will enable accurate reproduction of the disease state and more rigorous elucidation of genotype–phenotype correlations in hereditary disorders.

MATERIALS AND METHODS

Request a protocol through *Bio-protocol*.

Plasmids, antibodies, reagents, and cell lines

Expression vectors for subunits of the IFT-A and IFT-B complexes and heterotrimeric kinesin-II used in this study are listed in Supplemental Table S1; most of them were constructed in our previous studies (Katoh *et al.*, 2016; Hirano *et al.*, 2017; Funabashi *et al.*, 2018). The antibodies used in this study are listed in Supplemental Table S2. GST-tagged anti-GFP Nb (Katoh *et al.*, 2015) and anti-mCherry Nb (the LaM-2 version) (Ishida *et al.*, 2021) prebound to Glutathione Sepharose 4B beads (GE Healthcare) were prepared as described previously. SAG and Polyethylenimine Max were purchased from Enzo Life Sciences and Polysciences, respectively. HEK293T cells (RBC2202) and hTERT-RPE1 cells (CRL-4000) were obtained from the RIKEN BioResource Research Center and the American Type Culture Collection, respectively.

VIP assay and immunoblotting analysis

The VIP assay and subsequent immunoblotting analysis were performed by a previously described method (Katoh *et al.*, 2015, 2018) with minor modifications (Nishijima *et al.*, 2017); the experimental details are described elsewhere. In brief, approximately 8.0 $\times 10^5$ HEK293T cells were seeded onto six-well plates and cultured in DMEM with high glucose (Nacalai Tesque) supplemented with 5% fetal bovine serum (FBS). The next day, the cells were transfected with expression vectors for EGFP and mCherry fusion constructs using Polyethylenimine Max (20 µg) and cultured for 24 h. The cells were then lysed in 250 µl of cell lysis buffer (10 mM HEPES [pH 7.4], 5 mM $MgSO_4$, 1 mM dithiothreitol, 0.5 mM EDTA, 25 mM KCl, and 0.05% NP-40) containing EDTA-free protease inhibitor cocktail (Nacalai Tesque) for 20 min on ice and centrifuged at 16,100 × *g* for 15 min at 4°C in a microcentrifuge. The supernatants (200 µl) were incubated with 5 µl of GST-tagged anti-GFP Nb or anti-mCherry Nb (the LaM-2 version) prebound to Glutathione Sepharose 4B beads for 1 h at 4°C. The beads were washed three times with 180 µl of lysis buffer, transferred to a 96-well glass-bottomed plate (AGC Techno Glass), and observed using an all-in-one–type fluorescence microscope (BZ-8000; Keyence) using a 20×/0.75 objective lens under constant conditions (sensitivity ISO 400, exposure 1/20, 1/15, 1/10, 1/5, or 1/2 s for green fluorescence; and sensitivity ISO 800, exposure 1/50, 1/30, 1/20, 1/15, 1/10, or 1/2 s for red fluorescence).

After microscopy, the beads were boiled in SDS–PAGE sample buffer, and the proteins were separated by SDS–PAGE and electroblotted onto a TransBlot Turbo polyvinylidene difluoride membrane (Bio-Rad) or Immobilon-P membrane (Merck Millipore). The membrane was then blocked in 5% skimmed milk and incubated sequentially with primary antibody (anti-GFP or anti-mCherry) and peroxidase-conjugated secondary antibody. Protein bands were detected using a Chemi-Lumi One L kit (Nacalai Tesque), and images were captured with the Amersham ImageQuant 800 (Cytiva) or LAS-3000 (Fujifilm). The intensity of the bands was measured using ImageJ software. The original uncropped immunoblotting images are provided in the Supplemental "PowerPoint" file.

Establishment of *IFT52*-KO cell lines

The strategy for gene disruption of hTERT-RPE1 cells using the CRISPR/Cas9 system was as described previously (Katoh *et al.*, 2017) with minor modifications (Okazaki *et al.*, 2020; Fujisawa *et al.*, 2021). Briefly, single-guide RNA (sgRNA) sequences targeting the human *IFT52* gene (Supplemental Table S3) were designed using the CRISPOR tool (Haeussler *et al.*, 2016). Double-stranded oligonucleotides for the *IFT52* target sequences were inserted into the all-in-one sgRNA expression vector, pHiFiCas9-2 × sgRNA (Addgene no. 162277) (Fujisawa *et al.*, 2021; Noguchi *et al.*, 2021). hTERT-RPE1 cells were seeded onto a 12-well plate to approximately 1.5 × 10^5 cells, and the next day they were transfected with the sgRNA vector (1 µg) and the donor knock-in vector, pDonor-tBFP-NLS-Neo(universal) (0.25 µg; Addgene no. 80767) (Katoh *et al.*, 2017), using X-tremeGENE9 reagent (Roche). After selection by culturing the cells in the presence of G418 (600 µg/ml), the cells carrying tBFP signals were sorted using the SONY SH800S cell sorter at the Medical Research Support Center of Kyoto University. To detect the disruption of the *IFT52* gene, genomic DNAs extracted from the isolated cell lines were processed for PCR using GoTaq Master Mixes and three sets of primers (Supplemental Table S3) to distinguish the following three integration states of the donor knock-in vector: forward integration (Supplemental Figure S1, Ab and Cb'), reverse integration (Supplemental Figure S1, Ac and Cc'), and no integration with a small indel (Supplemental Figure S1, Aa and Ca'). The genomic PCR products were subjected to direct sequencing to confirm the disruption of both alleles of the *IFT52* gene (Supplemental Figure S1, B and D).

Preparation of *IFT52*-KO cells expressing mCherry-fused IFT52 constructs and EGFP-fused KIF17 or ICK

The preparation of lentiviral vectors was performed as described previously (Takahashi *et al.*, 2012; Ishida *et al.*, 2021). In brief, pRRLsinPPT-mCherry-IFT52(WT), pRRLsinPPT-mCherry-IFT52(Δ139–162), pRRLsinPPT-mCherry-IFT52(A199T), pRRLsinPPT-mCherry-IFT52(L293Afs*), or pRRLsinPPT-EGFP-ICK was transfected into HEK293T cells together with the packaging plasmids (pRSV-REV, pMD2.g, and pMDLg/pRRE [Thomas *et al.*, 2009]; kind gifts from Peter McPherson, McGill University). The culture medium was replaced 8 h after transfection and collected between 24 and 48 h after transfection. The lentiviral vector for EGFP-KIF17 was prepared as described previously (Funabashi *et al.*, 2017). The medium containing viral particles was passed through a 0.45-µm filter and then centrifuged at 32,000× *g* at 4°C for 4 h. Lentiviral particles precipitated from the medium were resuspended in DMEM/F-12 (Nacalai Tesque) and stored at –80°C until use. *IFT52*-KO cells expressing the mCherry-fused IFT52 construct were prepared by adding the lentiviral suspension to the culture medium, followed by selection in the presence of blasticidin (15 µg/ml) or Zeocin (10 µg/ml). *IFT52*-KO cells stably expressing the IFT52 construct were then infected with the lentiviral vector for EGFP-KIF17 or EGFP-ICK and selected in the presence of Zeocin (10 µg/ml).

Immunofluorescence analysis

Parental hTERT-RPE1 cells and *IFT52*-KO cells were cultured in DMEM/F-12 supplemented with 10% FBS and 0.348% sodium bicarbonate. The cells were grown to 100% confluence on coverslips and starved for 24 h in Opti-MEM (Invitrogen) containing 0.2% bovine serum albumin to induce ciliogenesis. Subsequent immunofluorescence analysis was performed as described previously (Ishida *et al.*, 2021; Zhou *et al.*, 2022). The cells were fixed and permeabilized with 3% paraformaldehyde at 37°C for 5 min and subsequently in methanol at –20°C for 5 min and then washed three times with phosphate-buffered saline. The fixed/permeabilized cells were blocked with 10% FBS and stained with antibodies diluted with 5% FBS. The stained cells were observed using an Axio Observer microscope (Carl Zeiss).

Quantification and statistical analysis

Quantification of fluorescence intensities and statistical analyses were performed as described previously (Qiu *et al.*, 2022; Zhou *et al.*, 2022). Briefly, all images acquired under the same setting were analyzed using ZEN 3.1 software (Carl Zeiss). The fluorescence intensity in a region of interest constructed along the signal of ARL13B or acetylated α-tubulin (Ac-tubulin) using a drawing tool was quantified. To correct for local background intensity, the fluorescence intensity of a nearby region was subtracted. Statistical analyses were performed using GraphPad Prism8 (version 8.4.3; GraphPad Software).

ACKNOWLEDGMENTS

We thank Peter McPherson for providing the plasmids for the production of recombinant lentiviruses and Helena Akiko Popiel for critical reading of the manuscript. This work was supported in part by grants from the Japan Society for the Promotion of Science (JSPS; grant numbers 19H00980 and 20H04904 to K. N., 18H02403 and 21H02427 to Y. K., and 22J20116 to Y. I.); and a grant of Joint Research Projects-LEAD with UK Research and Innovation from the JSPS (grant number JPJSJRP20181701 to K. N.). Y. I. was supported by a JSPS Research Fellowship.

REFERENCES

Anvarian Z, Mykytyn K, Mukhopadhyay S, Pedersen LB, Christensen ST (2019). Cellular signaling by primary cilia in development, organ function and disease. Nat Rev Nephrol 15, 199–219.

Boldt K, van Reeuwijk J, Lu Q, Koutroumpas K, Nguyen TM, Texier Y, van Beersum SEC, Horn N, Willer JR, Mans D, *et al.* (2016). An organelle-specific protein landscape identifies novel diseases and molecular mechanisms. Nat Commun 7, 11491.

Brown JM, Witman GB (2014). Cilia and diseases. BioScience 64, 1126–1137.

Bujakowska KM, Zhang Q, Siemiakowska AM, Liu Q, Place E, Falk MJ, Consugar M, Lancelot M-E, Antonio A, Lonjou C, *et al.* (2015). Mutations in *IFT172* cause isolated retinal degeneration and Bardet-Biedl syndrome. Hum Mol Genet 24, 230–242.

Dupont MA, Humbert C, Huber C, Siour Q, Guerrera IC, Jung V, Christensen A, Pouliet A, Garfa-Traoré M, Nitschké P, *et al.* (2019). Human IFT52 mutations uncover a novel role for the protein in microtubule dynamics and centrosome cohesion. Hum Mol Genet 28, 2720–2737.

Eguether T, San Agustin JT, Keady BT, Jonassen JA, Liang Y, Francis R, Tobita K, Johnson CA, Abdelhamed ZA, Lo CW, Pazour GJ (2014). IFT27 links the BBSome to IFT for maintenance of the ciliary signaling compartment. Dev Cell 21, 279–290.

Fujisawa S, Qiu H, Nozaki S, Chiba S, Katoh Y, Nakayama K (2021). ARL3 and ARL13B GTPases participate in distinct steps of INPP5E targeting to the ciliary membrane. Biol Open 10, bio058843.

Funabashi T, Katoh Y, Michisaka S, Terada M, Sugawa M, Nakayama K (2017). Ciliary entry of KIF17 is dependent on its binding to the IFT-B complex via IFT46-IFT56 as well as on its nuclear localization signal. Mol Biol Cell 28, 624–633.

Funabashi T, Katoh Y, Okazaki M, Sugawa M, Nakayama K (2018). Interaction of heterotrimeric kinesin-II with IFT-B-connecting tetramer is crucial for ciliogenesis. J Cell Biol 217, 2867–2876.

Garcia-Gonzalo FR, Reiter JF (2017). Open sesame: how transition fibers and the transition zone control ciliary composition. Cold Spring Harb Perspect Biol 9, a028134.

Girisha KM, Shukla A, Trujillano D, Bhavani GS, Hebbar M, Kadavigere R, Rolfs A (2016). A homozygous nonsense variant in *IFT52* is associated with a human skeletal ciliopathy. Clin Genet 90, 536–539.

Gonçalves J, Pelletier L (2017). The ciliary transition zone: finding the pieces and assembling the gate. Mol Cells 40, 243–253.

Haeussler M, Schönig K, Eckert H, Eschstruth A, Mianné J, Renaud JB, Schneider-Maunoury S, Shkumatava A, Teboul L, Kent J, *et al.* (2016). Evaluation of off-target and on-target scoring algorithms and integration into the guide RNA selection tool CRISPOR. Genome Biol 17, 148.

Hirano M, Satake W, Moriyama N, Saida K, Okamoto N, Cha P-C, Suzuki Y, Kusunoki S, Toda T (2020). Bardet-Biedl syndrome and related disorders in Japan. J Hum Genet 65, 847–853.

Hirano T, Katoh Y, Nakayama K (2017). Intraflagellar transport-A complex mediates ciliary entry and retrograde trafficking of ciliary G protein-coupled receptors. Mol Biol Cell 28, 429–439.

Ishida Y, Kobayashi T, Chiba S, Katoh Y, Nakayama K (2021). Molecular basis of ciliary defects caused by compound heterozygous *IFT144/WDR19* mutations found in cranioectodermal dysplasia. Hum Mol Genet 30, 213–225.

Katoh Y, Michisaka S, Nozaki S, Funabashi T, Hirano T, Takei R, Nakayama K (2017). Practical method for targeted disruption of cilia-related genes by using CRISPR/Cas9-mediated homology-independent knock-in system. Mol Biol Cell 28, 898–906.

Katoh Y, Nakamura K, Nakayama K (2018). Visible immunoprecipitation (VIP) assay: a simple and versatile method for visual detection of protein-protein interactions. Bio Protoc 8, e2687.

Katoh Y, Nozaki S, Hartanto D, Miyano R, Nakayama K (2015). Architectures of multisubunit complexes revealed by a visible immunoprecipitation assay using fluorescent fusion proteins. J Cell Sci 128, 2351–2362.

Katoh Y, Terada M, Nishijima Y, Takei R, Nozaki S, Hamada H, Nakayama K (2016). Overall architecture of the intraflagellar transport (IFT)-B complex containing Cluap1/IFT38 as an essential component of the IFT-B peripheral subcomplex. J Biol Chem 291, 10962–10975.

Kobayashi T, Ishida Y, Hirano T, Katoh Y, Nakayama K (2021). Cooperation of the IFT-A complex with the IFT-B complex is required for ciliary retrograde protein trafficking and GPCR import. Mol Biol Cell 32, 45–56.

Kopinke D, Norris AM, Mukhopadhyay S (2021). Developmental and regenerative paradigms of cilia regulated hedgehog signaling. Sem Cell Dev Biol 110, 89–103.

Liew GM, Ye F, Nager AR, Murphy JP, Lee JSH, Aguiar M, Breslow DK, Gygi SP, Nachury MV (2014). The intraflagellar transport protein IFT27 promotes BBSome exit from cilia through the GTPase ARL6/BBS3. Dev Cell 31, 265–278.

McInerney-Leo AM, Harris JE, Marshall MS, Gardiner B, Kinning E, Leong HY, McKenzie F, Ong WP, Vodopiutz J, Wicking C, *et al.* (2015). Whole exome sequencing is an efficient, sensitive and specific method for determining the genetic cause of short-rib thoracic dystrophies. Clin Genet 88, 550–557.

Nachury MV, Mick DU. (2019). Establishing and regulating the composition of cilia for signal transduction. Nat Rev Mol Cell Biol 20, 389–405.

Nakamura K, Noguchi T, Takahara M, Omori Y, Furukawa T, Katoh Y, Nakayama K (2020). Anterograde trafficking of ciliary MAP kinase-like ICK/CILK1 by the intraflagellar transport machinery is required for intraciliary retrograde protein trafficking. J Biol Chem 295, 13363–13376.

Nakayama K, Katoh Y (2018). Ciliary protein trafficking mediated by IFT and BBSome complexes with the aid of kinesin-2 and dynein-2 motors. J Biochem 163, 155–164.

Nakayama K, Katoh Y (2020). Architecture of the IFT ciliary trafficking machinery and interplay between its components. Crit Rev Biochem Mol Biol 55, 179–196.

Nishijima Y, Hagiya Y, Kubo T, Takei R, Katoh Y, Nakayama K (2017). RABL2 interacts with the intraflagellar transport B complex and CEP19 and participates in ciliary assembly. Mol Biol Cell 28, 1652–1666.

Noguchi T, Nakamura K, Satoda Y, Katoh Y, Nakayama K (2021). CCRK/CDK20 regulates ciliary retrograde protein trafficking via interacting with BROMI/TBC1D32. PLoS ONE 16, e0258497.

Okazaki M, Kobayashi T, Chiba S, Takei R, Liang L, Nakayama K, Katoh Y (2020). Formation of the B9-domain protein complex MKS1–B9D2–B9D1 is essential as a diffusion barrier for ciliary membrane proteins. Mol Biol Cell 31, 2259–2268.

Porto EM, Komor AC, Slaymaker IM, Yeo GW (2020). Base editing: advances and therapeutic opportunities. Nat Rev Drug Discov 19, 839–859.

Prevo B, Scholey JM, Peterman EJG (2017). Intraflagellar transport: mechanisms of motor action, cooperation, and cargo delivery. FEBS J 284, 2905–2931.

Qiu H, Tsurumi Y, Katoh Y, Nakayama K (2022). Combinations of deletion and missense variations of the dynein-2 DYNC2LI1 subunit found in skeletal ciliopathies cause ciliary defects. Sci Rep 12, 31.

Reiter JF, Leroux MR (2017). Genes and molecular pathways underpinning ciliopathies. Nat Rev Mol Cell Biol 18, 533–547.

Satoda Y, Noguchi T, Fujii T, Taniguchi A, Katoh Y, Nakayama K (2022). BROMI/TBC1D32 together with CCRK/CDK20 and FAM149B1/JBTS36 contributes to IFT turnaround involving ICK/CILK1. Mol Biol Cell 33, 1–14.

Schaefer E, Stoetzel C, Scheidecker S, Geoffroy V, Prasad MK, Redin C, Missotte I, Lacombe D, Mandel J-L, Muller J, Dollfus H (2016).

Identification of a novel mutation confirms the implication of *IFT172* (*BBS20*) in Bardet-Biedl syndrome. J Hum Genet 61, 447–450.
Schmidts M (2014). Clinical genetics and pathobiology of ciliary chondrodysplasias. J Pediatr Genet 3, 49–64.
Schmidts M, Hou Y, Cortés C, Mans DA, Huber C, Boldt K, Patel M, van Reeuwijk J, Plaza JM, van Beersum SEC, *et al*. (2015). TCTEX1D2 mutations underlie Jeune asphyxiating thoracic dystrophy with impaired retrograde intraflagellar transport. Nat Commun 6, 7074.
Takahara M, Katoh Y, Nakamura K, Hirano T, Sugawa M, Tsurumi Y, Nakayama K (2018). Ciliopathy-associated mutations of IFT122 impair ciliary protein trafficking but not ciliogenesis. Hum Mol Genet 27, 516–528.
Takahashi S, Kubo K, Waguri S, Yabashi A, Shin H-W, Katoh Y, Nakayama K (2012). Rab11 regulates exocytosis of recycling vesicles at the plasma membrane. J Cell Sci 125, 4049–4057.
Takei R, Katoh Y, Nakayama K (2018). Robust interaction of IFT70 with IFT52–IFT88 in the IFT-B complex is required for ciliogenesis. Biol Open 7, bio033241.
Taschner M, Bhogaraju S, Vetter M, Morawetz M, Lorentzen E (2011). Biochemical mapping of interactions within the intraflagellar transport (IFT) B core complex: IFT52 binds directly to four other IFT-B subunits. J Biol Chem 286, 26344–26352.
Taschner M, Kotsis F, Braeuer P, Kuehn EW, Lorentzen E (2014). Crystal structures of IFT70/52 and IFT52/46 provide insight into intraflagellar transport B core complex assembly. J Cell Biol 207, 269–282.
Taschner M, Weber K, Mourão A, Vetter M, Awasthi M, Stiegler M, Bhogaraju S, Lorentzen E (2016). Intraflagellar transport proteins 172, 80, 57, 54, 38, and 20 form a stable tubulin-binding IFT-B2 complex. EMBO J 35, 773–790.
Thomas S, Ritter B, Verbich D, Sanson C, Bourbonnière L, McKinney RA, McPherson PS (2009). Intersectin regulates dendritic spine development and somatodendritic endocytosis but not synaptic vesicle recycling in hippocampal neurons. J Biol Chem 284, 12410–12419.
Tunyasuvunakool K, Adler J, Wu Z, Green T, Zielinski M, Žídek A, Bridgland A, Cowie A, Meyer C, Laydon A, *et al*. (2021). Highly accurate protein structure prediction for the human proteome. Nature 596, 590–596.
Zhang W, Taylor SP, Ennis HA, Forlenza KN, Duran I, Li B, Ortiz Sanchez JA, Nevarez L, Nickerson DA, Bamshad M, *et al*. (2018). Expanding the genetic architecture and phenotypic spectrum in the skeletal ciliopathy. Hum Mut 39, 152–166.
Zhang W, Taylor SP, Nevarez L, Lachman RS, Nickerson DA, Bamshad M, University of Washington Center for Mendelian Genomics Consortium, Krakow D, Cohn DH (2016). IFT52 mutations destabilize anterograde complex assembly, disrupt ciliogenesis and result in short rib polydactyly syndrome. Hum Mol Genet 25, 4012–4020.
Zhou Z, Qiu H, Castro-Araya R-F, Takei R, Nakayama K, Katoh Y (2022). Impaired cooperation between IFT74/BBS22–IFT81 and IFT25–IFT27/BBS19 in the IFT-B complex causes ciliary defects in Bardet-Biedl syndrome. Hum Mol Genet 31, 1681–1693.